



Research paper

Superior oxygen transfer ability of Pd/MnO_x-CeO₂ for enhanced low temperature CO oxidation activity

Chao Wang, Cun Wen, Jochen Lauterbach, Erdem Sasmaz*

Smartstate Center for Strategic Approaches to The Generation of Electricity (SAGE), Department of Chemical Engineering, University of South Carolina, Columbia, SC, 29208, USA

ARTICLE INFO

Article history:

Received 27 September 2016

Received in revised form 4 January 2017

Accepted 5 January 2017

Available online 6 January 2017

Keywords:

Pd

Low temperature CO oxidation

Oxygen transfer

Metal-support interaction

ABSTRACT

The low temperature CO oxidation activity of Pd doped MnO_x-CeO₂ (MC) solid solution catalyst is evaluated to determine the role of Pd speciation and oxygen transfer. Dynamic reduction behavior of Pd²⁺ species in the presence of CO at low temperatures is characterized by in-situ diffuse reflectance infrared Fourier transform spectroscopy (DRIFTS) and X-ray absorption spectroscopy (XAS). H₂ temperature-programmed reduction (TPR) and CO/O₂ transient pulse experiments are conducted to evaluate the lattice oxygen reducibility of Pd/CeO₂ and Pd/MC.

Our results show that highly dispersed PdO species form on the freshly calcined CeO₂ and MC supports. Despite the fact that similar Pd species form on the CeO₂ and MC supports, PdO can be reduced immediately on CeO₂ in the presence of CO, while the MC support can preserve the oxidized Pd species during CO reduction. In the case of CO oxidation, Pd²⁺ species are maintained through lattice oxygen transfer facilitated by the MC support. CO/O₂ transient pulse experiments confirm the higher reducibility of the MC support, which can favor CO oxidation at 50 °C.

© 2017 Elsevier B.V. All rights reserved.

1. Introduction

Carbon monoxide is a toxic pollutant and produced due to the incomplete combustion of carbon-containing fuels [1,2]. The majority of CO emissions come from mobile sources and catalytic oxidation of CO is the most widely used control technology to remediate CO emissions [2]. Even though the current commercialized platinum group metal (PGM) catalysts can reduce most of the CO content at temperatures above 200 °C, up to 80% of CO is still emitted during the cold-start stage of a vehicle due to the low operating temperature of the catalyst [2–4].

CeO₂ is a widely used component in mobile emission control catalysts due to the Ce³⁺/Ce⁴⁺ redox cycle [5–17]. CeO₂ can utilize lattice oxygen reversibly for CO oxidation depending on the exhaust gas composition, improve the dispersion of noble metals and enhance catalyst stability at high temperatures [5]. All these promoting effects shift the light-off temperature for CO oxidation to lower operating temperatures and provide a stable catalyst structure [6–17]. Addition of a PGM on CeO₂ as an active phase can create adsorption sites for CO and promote CO oxidation [12,16]. Among

the PGMs, Pd based CeO₂ catalysts are shown to have fast light-off performance, high oxidation capability, and better sintering resistance [17]. The low CO oxidation activity of the Pd/CeO₂ catalyst can be attributed to the existence of small PdO nanoparticles and Pd²⁺ ions in the form of a Ce_{1-x}Pd_xO_{2-δ} solid solution. Both of these Pd species can be obtained via conventional synthesis techniques, such as wet impregnation, co-precipitation, and solution combustion [11,15,16,18,19]. Pd²⁺ ions substituted into the CeO₂ framework by solution combustion show better CO oxidation activity at temperatures below 120 °C if compared to the Pt, and Rh metal ions [7]. However, up to 94% of Pd content in the solution combustion synthesis remains in the bulk and may have a little contribution to CO oxidation [15,16]. On the other hand, conventional wet impregnation can concentrate most of the Pd species on the CeO₂ surface, while still maintaining a high CO oxidation activity at low temperatures [18].

Incorporation of a secondary base metal (i.e. Fe, Zr, Sn, Ti, Mn) into the CeO₂ framework can further enhance the CO oxidation activity [7,20,21]. The promotional effect of the secondary metal can be attributed to the superior redox cycle and oxygen storage capacity of the support due to the lattice distortion and formation of charge-compensating oxygen vacancies [6,20,22]. In our recent work, Mn incorporated Pd/CeO₂ catalyst synthesized via wet impregnation and co-precipitation show excellent CO oxidation activity at ambient temperatures and maintained its stability

* Corresponding author at: 541 Main St., Room 136, Horizon I, Columbia, SC, 29201, USA.

E-mail address: sasmaz@cec.sc.edu (E. Sasmaz).

even after hydrothermal treatment at 750 °C [20]. Further tests performed over the Pd/MnO_x-CeO₂ (Pd/MC) catalyst under diesel exhaust gas conditions reveals that high CO and hydrocarbons oxidation can be achieved at temperatures below 200 °C [22].

Through our studies, the role of Pd speciation and support to low temperature CO oxidation activity of the Pd deposited MC support could not be clarified. In addition, the dynamic change in Pd structure during CO oxidation on CeO₂ and MC needs to be elucidated to determine metal-support interaction. In this work, the low temperature CO oxidation activity of Pd doped MC solid solution catalysts is investigated by means of in-situ X-ray absorption spectroscopy (XAS) and X-ray photoelectron spectroscopy (XPS). Dynamic reduction behavior of Pd²⁺ species in the presence of CO at low temperatures is characterized by in-situ diffuse reflectance infrared Fourier transform spectroscopy (DRIFTS). H₂ temperature-programmed reduction (TPR) and CO/O₂ transient pulse experiments are conducted to evaluate the lattice oxygen reducibility of Pd/CeO₂ and Pd/MC.

2. Experiments

2.1. Catalysts synthesis

The MC supports were prepared by an ultrasonic assisted co-precipitation method, where Mn(NO₃)₂ and Ce(NO₃)₃, with a mole ratio of 1:1, were used as the catalyst precursors and (NH₄)₂CO₃ (1 mol L⁻¹) as a precipitator. The paste obtained from co-precipitation was treated by ultrasound for 2 h, followed by subsequent filtration. The samples were then washed with deionized water, dried in stagnant air overnight at 105 °C, and calcined in stagnant air at 500 °C for 6 h. Pd/MC with 1 wt% Pd loading was synthesized by impregnation. The MC support was immersed in aqueous Pd(NO₃)₂ solution and dried at room temperature while stirring. Then the solid was calcined in stagnant air at 550 °C for 3 h. Similarly, Pd/CeO₂ was synthesized using the precipitation and impregnation method. The Ce(NO₃)₃ precursor was only mixed with the (NH₄)₂CO₃ (1 mol L⁻¹) precipitator and synthesized following the aforementioned procedure described for Pd/MC. The actual Pd loadings of Pd/MC and Pd/CeO₂ were measured by atomic absorption spectroscopy, and found to be 1.1 ± 0.05 wt% and 1.0 ± 0.05 wt%, respectively. Additionally, 5 wt% and 0.5 wt% Pd/CeO₂, and 5 wt% Pd/MC samples were synthesized as a reference sample to compare Pd speciation. The Pd loading on 5 wt% samples were measured to be 5.1 ± 0.05 wt% and 4.4 ± 0.05 wt% on Pd/MC and Pd/CeO₂, respectively. The actual Pd loading on 0.5 wt% Pd/CeO₂ was 0.49 ± 0.05 wt%.

2.2. Catalytic testing

CO oxidation experiments were conducted in a plug flow reactor under atmospheric pressure. A gas mixture of 2.0% CO (99.999% CO, Airgas), 5% O₂ (99.9999% O₂, Airgas) and balance Ar (99.9999% Ar, Airgas) was fed to the reactor via mass flow controllers (Brooks 5850E). 200 mg of catalyst supported with quartz wool was placed in the reactor for each run and no pretreatment was performed before the reaction. The catalyst temperature was recorded using a thermocouple placed inside the catalyst bed. The gas hourly space velocity (GHSV) for all experiments was 40,000 h⁻¹. The amount of CO before and after the reaction was measured using a differentially pumped mass spectrometer (MS, Hiden HAL IV RC). CO conversion was reported at steady state at each temperature and calculated by using the following formula: (CO_{inlet} - CO_{outlet})/CO_{inlet}, where CO_{inlet} and CO_{outlet} represent the concentration of CO inlet and outlet of the reactor, respectively. The conversion error is calculated to be less than ±5% after repetitive tests.

The turnover frequency (TOF) of the Pd catalysts was calculated by using the following equation:

$$TOF = \frac{F * X}{n(Pd)}$$

where F is the flow rate of CO in mol s⁻¹, X is the CO conversion at 50 °C, and n(Pd) is the mole of Pd in the catalyst.

2.3. Catalyst characterization

Powder X-ray diffraction (XRD) data for fresh samples were collected on a RigakuMiniflex II desktop diffractometer using a Cu Kα source with D/teX Ultra 250 silicon strip detector. XPS was carried out on a Kratos AXIS Ultra DLD XPS system equipped with a hemispherical energy analyzer. A monochromatic Al Kα X-ray source (1486.6 eV) was operated at 15 kV and 120 W. All spectra were calibrated to the adventitious carbon at 284.8 eV (C1s). The high-resolution elemental mapping and imaging of particles were collected using a FEI Talos F200X scanning transmission electron microscope (STEM).

XAS was collected at X-ray beamline 4-1 at the Stanford Synchrotron Radiation Lightsource (SSRL), Menlo Park, CA. The storage ring electron energy was 3 GeV with a current of 500 mA. Pd K-edge spectra were collected in the transmission mode with a Si (220) double-crystal monochromator that was detuned by 30% to minimize effects of higher harmonics in the X-ray beam. A Pd foil reference compound was placed between the I₁ and I₂ ion chambers to serve as a continuous energy calibration standard. A reference sample (PdO, 50 mg, Sigma-Aldrich) was mixed with boron nitride (BN, Sigma-Aldrich) (150 mg) to give an appropriate absorbance at the edge energy, whereas other samples (200 mg) were used without mixing with BN. Samples were then hand pressed inside the sample holder and loaded into the reaction cell, which was then evacuated down to 10⁻⁵ Torr [23]. PdO were cooled down using a liquid N₂ cryostat and the Pd K-edge XAS of the sample was collected. Both Pd/CeO₂ and Pd/MC samples were first exposed to He at room temperature (ca. 25 °C) for 1.5 h. Subsequently, 1% CO and 0.7% O₂ balanced with He was introduced into the cell. The in-situ reaction was conducted at the reaction cell temperatures of room temperature (RT), 50 °C and 100 °C. Pd K-edge XAS of the samples was collected at each condition. The X-ray absorption near edge structure (XANES) analysis of the samples was performed using the Athena software [24].

Time resolved DRIFTS experiments were performed on a Bruker Equinox 55 spectrometer equipped with a deuterated triglycine sulfate (DTGS) detector. CO adsorption was performed over the Pd/CeO₂ and Pd/MC samples at 50 °C and atmospheric pressure. 2% CO balanced with Ar was injected to the reaction cell at a total flow rate of 50 sccm for 10 min. The sample spectra were collected during CO adsorption with an accumulation of 32 scans at a resolution of 4 cm⁻¹. Background spectra were collected in Ar without the presence of CO.

The reduction properties of the catalysts were characterized through H₂-TPR experiments. 200 mg of a catalyst supported with quartz wool was placed in a quartz tube and no additional pretreatment was performed. A reduction gas of 10% H₂ balanced with Ar was introduced with a flow rate of 50 ml min⁻¹. The sample was heated up to 800 °C with a rate of 10 °C min⁻¹. H₂ consumption was monitored by a differentially pumped MS and calculated by integrating the peak area.

CO/O₂ transient pulse experiments were conducted in the aforementioned plug flow reactor used for CO oxidation experiments. 200 mg of the 1 wt% Pd/CeO₂ and Pd/MC catalysts were placed in the reactor and tested under the flow rate of 100 sccm. Initially, the catalysts were pretreated with 5% O₂ for 30 min at 50 °C. Subsequently,

the catalyst was purged with pure Ar for 30 min. Following the pre-treatment, 2% CO balanced with Ar and 5% O₂ balanced with Ar were each cycled to the reactor every 10 min. Between each pulse, pure Ar was introduced to purge the residual gas for 10 min. The CO₂ (m/e = 44), O₂ (m/e = 32), CO (m/e = 28), and Ar (m/e = 40) signals were monitored by the differentially pumped MS.

3. Results and discussion

3.1. Catalysts structure characterization

XRD was carried out to analyze the crystal structure of the samples. As shown in Fig. 1, the observed diffraction patterns in all samples can be attributed to the (111), (200), (220), (311) and (222) lattice planes of the cubic fluorite structure of CeO₂, indicating that Mn and Ce form a solid solution without appreciable phase separation [20]. The change in the lattice parameter of CeO₂ after Mn addition and the physical properties (particle size, surface area, pore size) of Pd/CeO₂ and Pd/MC have been discussed in detail and published elsewhere [20,22]. The 1 wt% Pd/CeO₂ and Pd/MC catalysts do not show any diffraction peaks corresponding to Pd metal (40.2°) or PdO (34°, 42°) [18,20,22]. The lack of Pd diffraction peaks can be due to the small amount of Pd loading or formation of highly dispersed small Pd nanoparticles [16,18]. Indeed, increasing Pd loading to 5 wt% on MC leads to the formation of a weak diffraction peak at 42°, corresponding to crystalline PdO [18]. In the case of 5 wt% Pd/CeO₂, an even weaker diffraction peak at 42° is observed. The broader full width at half maximum of the PdO peak for the Pd/CeO₂ sample indicates that smaller PdO nanoparticles might be forming on Pd/CeO₂ in comparison to Pd/MC.

The morphology and elemental distribution of Ce, Mn, and Pd in the 1 wt% Pd/MC catalyst are determined by STEM, as shown in Fig. 2. The freshly calcined sample comprises nanoparticles with

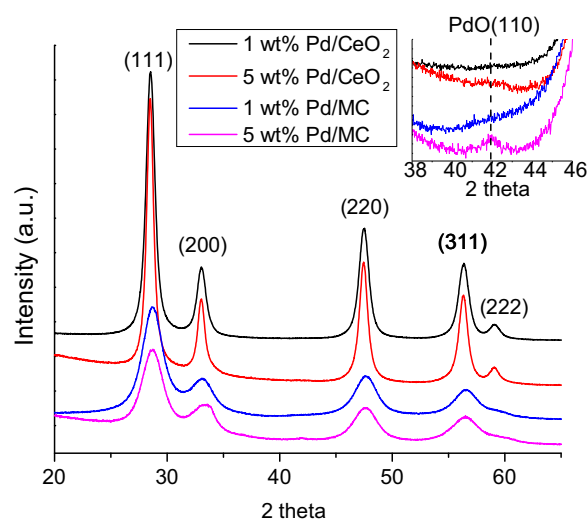


Fig. 1. XRD of the calcined 1 wt% and 5 wt% Pd catalysts.

spherical or elliptical shapes and sizes in the range of 20 and 40 nm. The high-resolution elemental mapping of the Pd/MC sample indicates that all Ce and Mn are uniformly distributed within the sample structure, confirming the formation of a Mn-Ce solid solution. Pd mapping clearly shows that Pd is highly dispersed on the MC support, in consistent with XRD results.

XPS was conducted to investigate Pd oxidation state and speciation on the CeO₂ and MC supports. As shown in Fig. 3, the 3d_{5/2} peak of the PdO reference sample locates at 336.6 ± 0.2 eV with a full width half maximum (FWHM) of 1.16 eV, which is consistent with the literature [7]. The Pd 3d_{5/2} peak of 1 wt% Pd-CeO₂ can be deconvoluted into two peaks at 337.7 ± 0.2 and 336.5 ± 0.2 eV with

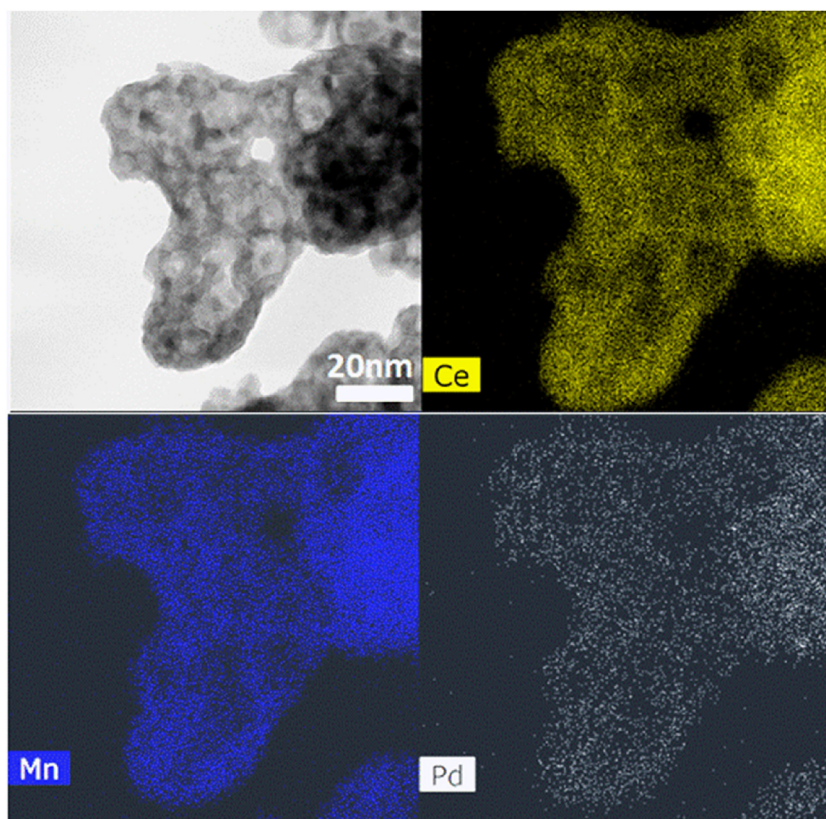


Fig. 2. STEM images and high-resolution elemental mapping of the calcined 1 wt% Pd/MC.

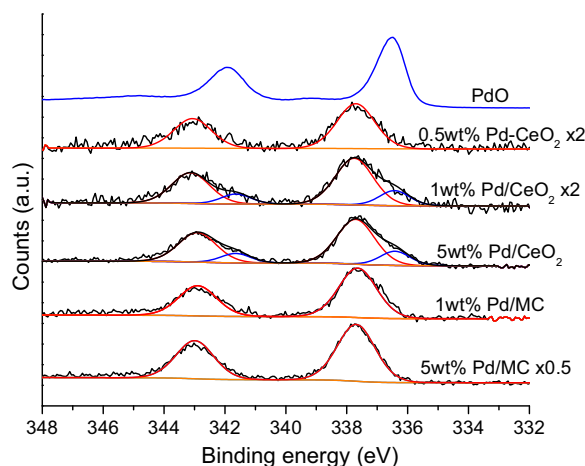


Fig. 3. Pd 3d core-level XPS of the calcined Pd catalysts.

a FWHM of 1.46 eV and 1.16 eV, respectively. In the case of 1 wt% Pd/MC, only a high binding energy peak is detected at 337.7 eV with a FWHM of 1.46 eV. The lower binding energy peak at 336.5 ± 0.2 eV is similar to the PdO reference sample and can be attributed to the crystalline PdO phase, while the higher binding energy peak might be due to the formation of highly dispersed Pd^{2+} species or $\text{Pd}_x\text{Ce}_{1-x}\text{O}_{2-\delta}$ interaction phase [9,10,25,26]. The crystalline PdO phase observed on 1 wt% Pd/CeO₂ accounts for 21% of the total Pd amount. As shown in Fig. 3, increasing Pd loading to 5 wt% on CeO₂ and MC does not affect Pd speciation. The 5 wt% Pd samples show similar Pd 3d core level spectra as the 1 wt% Pd samples. With the increased Pd loading, the MC support can still maintain all Pd species at a high Pd 3d_{5/2} binding energy of 337.7 ± 0.2 eV. The 1.1 eV binding energy shift compared to the PdO reference sample could be due to the particle size influence on metal binding energy that arises from final-state screening effects. As the particle size decreases, the d-electrons are more localized and become less effective to screen the hole created by the photoemission. This effect leads to a decrease in relaxation energy of the final state and thereby increases the apparent binding energy [27–29]. As the Pd loading is decreased to 0.5 wt% on CeO₂, the Pd 3d binding energy for crystalline PdO phase disappears and only a high binding energy peak at 337.7 ± 0.2 eV, corresponding to highly dispersed PdO nanoparticles, is observed. These results indicate that highly dispersed PdO nanoparticles form first on the CeO₂ surface with the addition of small Pd loadings (0.5 wt%). The crystalline PdO phase forms at Pd loadings in between 0.5 wt% and 1 wt%, and its relative amount remains stable above Pd loadings of 1 wt%.

The oxidation state of Pd is further investigated through XAS experiments. Fig. 4 shows the Pd K-edge XANES spectra of the 1 wt% Pd/CeO₂ and Pd/MC samples in the presence of He at room temperature. Both Pd foil and PdO were characterized as a reference sample. As shown in Fig. 4, the absorption edge of the PdO is measured to be 24353 eV, which is consistent with the value in the literature [3]. In comparison to the XAS of the PdO reference sample, the Pd K-edge of Pd/CeO₂ and Pd/MC samples shifts to higher absorption energies by 0.6 ± 0.2 eV and 0.9 ± 0.2 eV, respectively. Such shifts are likely due to the chemical interaction of Pd^{2+} species with the support [30]. In any case, the absorption energy of the Pd K-edge for both Pd/CeO₂ and Pd/MC samples is above that of the Pd foil and shows similar features to the one of PdO. These results indicate that Pd is likely in the form of Pd^{2+} and no metallic palladium (Pd^0) exists in the freshly calcined samples. This is also in agreement with the XPS analysis, in which the Pd 3d_{5/2} binding energy at 335.3 eV corresponding to Pd^0 is not pronounced on the freshly calcined samples.

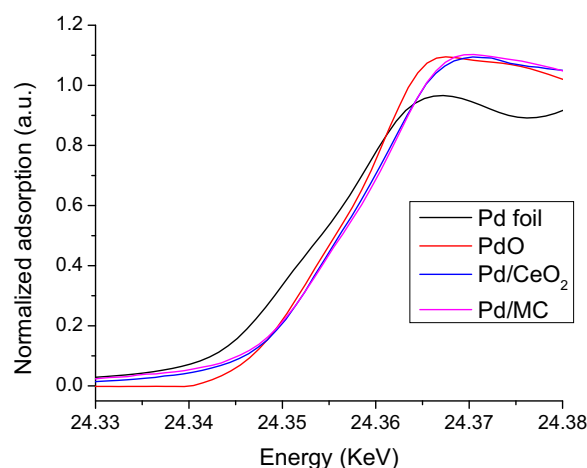


Fig. 4. Pd K-edge XANES spectra of 1 wt% Pd/CeO₂ and 1 wt% Pd/MC recorded in He flow at room temperature. PdO and Pd foil are shown as a reference.

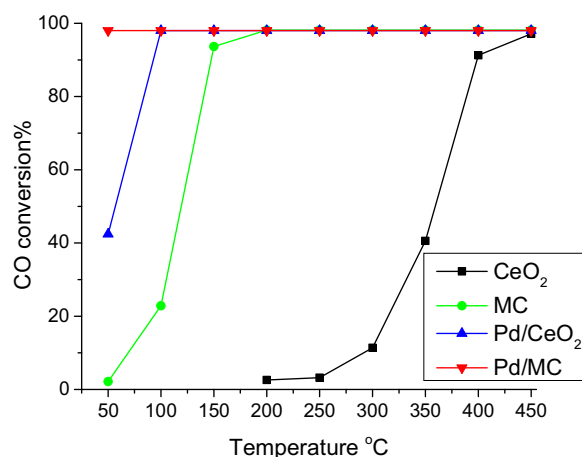


Fig. 5. CO oxidation activity of CeO₂, MC and 1 wt% Pd supported catalysts: CO/O₂ ratio of 2:5 and GHSV = 40,000 h⁻¹.

3.2. CO oxidation activity

Fig. 5 shows the catalytic activity of the CeO₂, MC, 1 wt% Pd/CeO₂ and 1 wt% Pd/MC samples for CO oxidation. The CeO₂ support has almost no catalytic activity for CO oxidation under 250 °C. After incorporation of Mn into the CeO₂ lattice, the T₉₀ (temperature at which 90% CO conversion occurs) of the MC support decreases from 400 °C to 150 °C. The promotional effect of Mn addition for CO oxidation is likely due to a redox cycle between $\text{Ce}^{3+}/\text{Ce}^{4+}$ and $\text{Mn}^{4+}/\text{Mn}^{3+}/\text{Mn}^{2+}$ ions, which increases the lattice oxygen mobility and redox property [31,32]. The improved oxygen mobility and redox property of the MC support could be associated with the decreased formation energy of oxygen vacancies [32]. It is proposed that the incorporation of Mn^{x+} ions into the CeO₂ (111) can decrease the single oxygen vacancy formation energy by inducing an unfilled $\text{Mn}_{3d}-\text{O}_{2p}$ gap state between the O 2p valance band and the Ce 4f conduction band [32]. After impregnation of 1 wt% Pd, the Pd/CeO₂ catalyst shows almost 100% CO conversion at 100 °C, but decreases to ca. 40% at 50 °C. In the case of Pd/MC, almost 100% of the CO is already converted at 50 °C and such high conversion is maintained with increasing temperature.

The TOFs of Pd/CeO₂ and Pd/MC can be calculated assuming that either all of the Pd content or highly dispersed Pd species are active for CO oxidation [15]. If all the Pd content on the support is active, the TOFs of Pd/CeO₂ and Pd/MC are found to be 0.032 s⁻¹ and

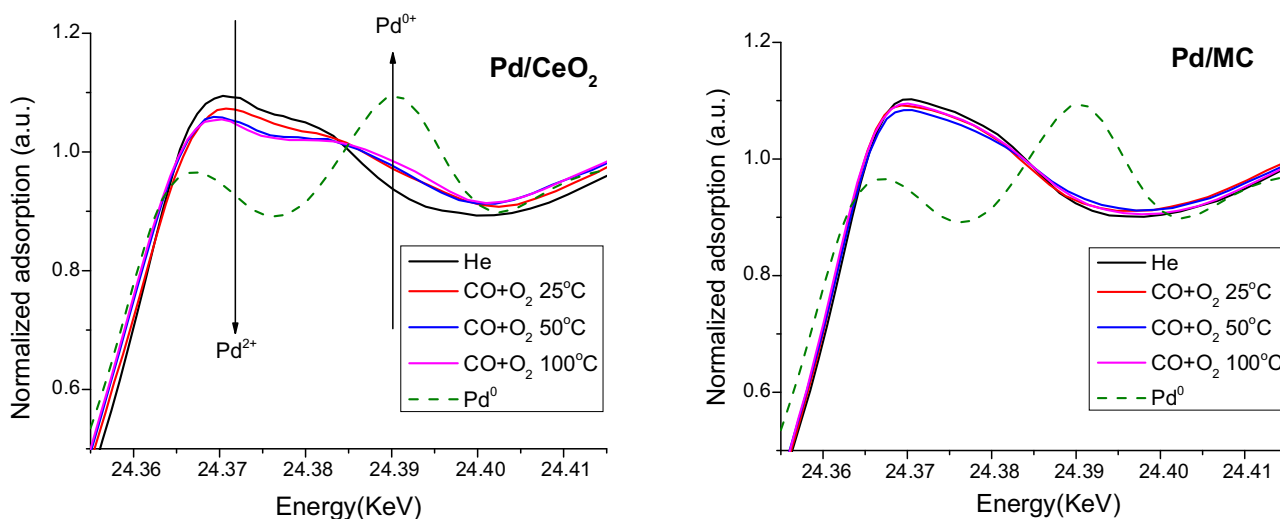


Fig. 6. Pd K-edge XANES spectra of 1 wt% Pd supported catalysts during CO oxidation.

Table 1

In situ XANES analysis of the Pd catalysts during He treatment and CO oxidation^a.

| Catalysts | Pd oxidation state | Percentage of Pd ²⁺ or Pd ⁰ at different conditions (%) | | | |
|---------------------|------------------------|---|-------------------------|-------------------------|--------------------------|
| | | He | CO+O ₂ 25 °C | CO+O ₂ 50 °C | CO+O ₂ 100 °C |
| Pd/CeO ₂ | Pd ²⁺ (±5%) | 100 | 72 | 68 | 62 |
| | Pd ⁰ (±5%) | 0 | 28 | 32 | 38 |
| Pd/MC | Pd ²⁺ (±5%) | 100 | 95 | 92 | 93 |
| | Pd ⁰ (±5%) | 0 | 5 | 8 | 7 |

^a The XANES spectra were fitted as a linear combination of the Pd foil spectra and the spectra of PdO reference.

0.072 s⁻¹ at 50 °C, respectively. Although the highly dispersed Pd species are considered as an active site, the TOF of Pd/CeO₂ slightly increases to 0.04 s⁻¹. These results indicate that CO conversion of Pd/CeO₂ and Pd/MC is not linearly correlated with the amount of highly dispersed PdO nanoparticles present on the surface, suggesting that the dispersion of PdO nanoparticles is not the only factor that controls the catalytic activity at low temperatures. CO oxidation is generally accepted to follow the Mars-Van Krevelen mechanism on the Pd-Ce based catalysts [33]. Active supports, e.g. CeO₂ and MC can participate the reaction by providing reactive lattice oxygen for CO oxidation [7]. Therefore, the high CO oxidation activity observed over Pd/MC could similarly be related with the lower oxygen vacancy formation energy [31,32]. To further understand the high activity observed over Pd/MC at low temperatures, a series of in-situ and ex-situ characterization experiments were conducted.

3.3. In-situ XAS experiments

In-situ XAS experiments were conducted over the 1 wt% Pd/CeO₂ and Pd/MC samples to determine the change in Pd oxidation state during CO oxidation. For these experiments, a higher CO:O₂ ratio (1:0.7) was employed compared to the reactor tests (Fig. 5). This higher CO:O₂ ratio is not expected to impact the CO conversion mechanism in the presence of excess oxygen, as the reaction order is reported to be positive and nearly zero with respect to CO and O₂ on Pd/CeO₂, respectively [33]. A linear combination fitting is employed to the XANES spectra of Pd/CeO₂ and Pd/MC via Pd foil and PdO reference samples to determine the change in the Pd oxidation state [34]. For the linear combination fitting, it is assumed that the Pd oxidation state is in 2+ and its local structure is in the form of PdO in Pd/CeO₂ and Pd/MC. As shown in Fig. 6 and Table 1, upon injection of CO and O₂ at RT, a new

feature appears at 24390 eV, corresponding to Pd⁰ in the Pd/CeO₂ spectra. The quantification of Pd⁰ formations on Pd/CeO₂ reveals that approximately 30 ± 5% of Pd²⁺ is reduced to Pd⁰ at 50 °C. In comparison, there is only slight change of the XANES spectra of Pd/MC upon CO oxidation and up to 8 ± 5% of Pd²⁺ is reduced to Pd⁰. This indicates that the MC support can maintain almost all the Pd content in the oxidized state during CO oxidation.

3.4. In-situ DRIFTS experiments

In-situ DRIFTS experiments were performed at 50 °C to evaluate the Pd adsorption sites during CO exposure over Pd/CeO₂ and Pd/MC. The IR spectra were collected as a function of time to determine the reducibility of the oxidized Pd sites on the supports. As shown in Fig. 7, Pd/CeO₂ shows a band at 2088 cm⁻¹ after 30 s of CO exposure, which is assigned to CO adsorbed on an atop site of Pd⁰ [35]. At the same time, a weak broad band appears between 1980 and 1800 cm⁻¹, corresponding to chemisorbed CO on Pd⁰ bridge (1980–1860 cm⁻¹) and threefold hollow sites (1920–1800 cm⁻¹) [36]. CO adsorbed on Pdⁿ⁺ sites in the range of 2150–2100 cm⁻¹ is not observed during these experiments, which could be due to the fast reduction of Pd²⁺ at high CO concentrations [22]. The integrated peak area of the IR bands for atop, bridge-hollow sites as well as gas phase CO₂ for both catalysts is plotted as a function of CO exposure time, as shown in Fig. 7c and 7d. Unlike Pd/CeO₂, Pd/MC shows significant gas phase CO₂ band in the first 30 s of CO exposure, meanwhile no bands for CO adsorbed on Pd⁰ sites could be detected. After 60 s of CO exposure, a band for CO adsorbed on atop Pd⁰ sites at 2092 cm⁻¹ begins to grow on the Pd/MC sample, while a broad band at 1980–1800 cm⁻¹, corresponding to bridge and hollow sites appears only after 120 s of CO exposure. As the reaction continues, the intensity of all these sites grows appreciably. In addition to the CO bands, carbonate species form on the

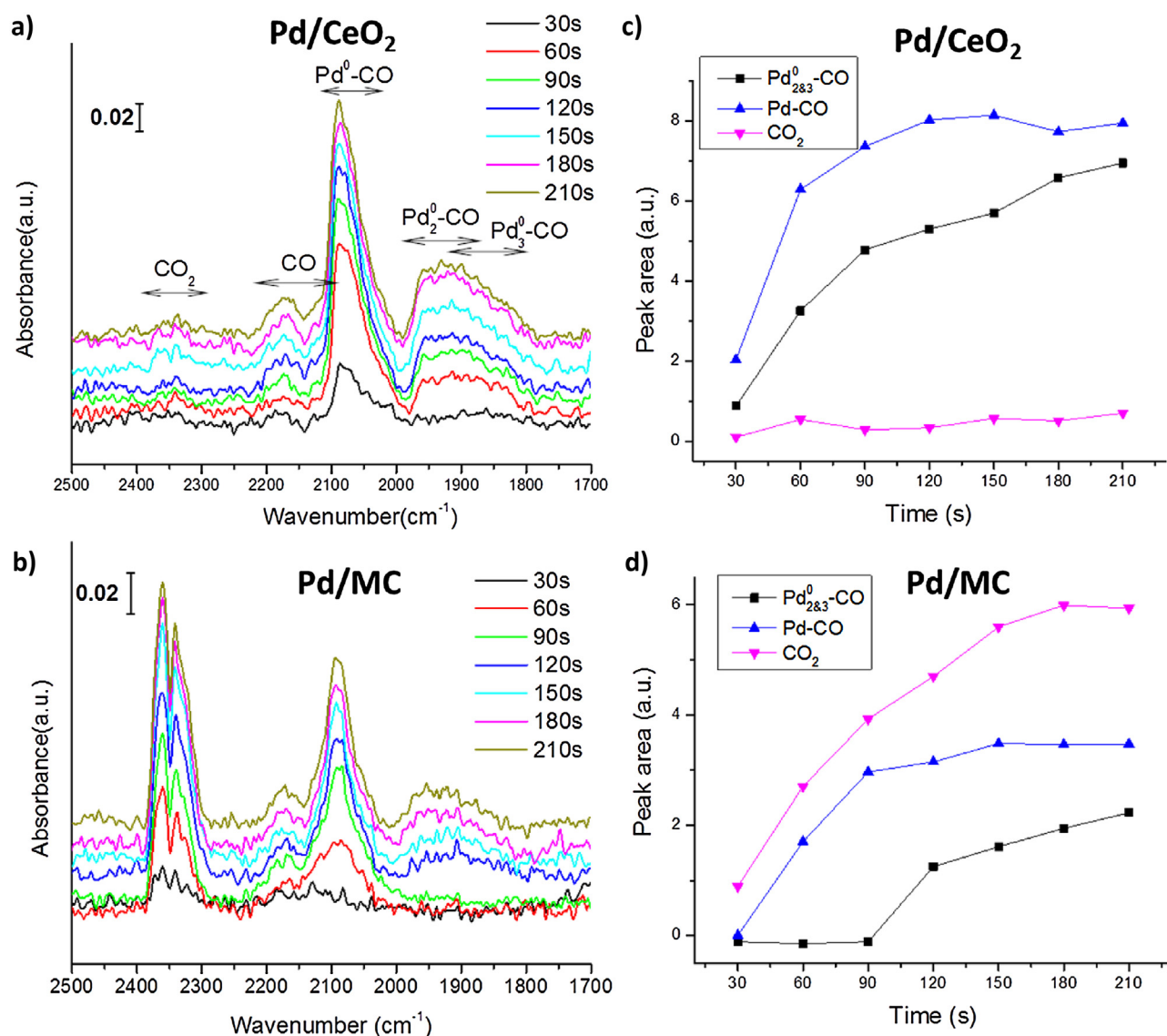


Fig. 7. a,b) Baseline corrected in-situ DRIFT spectra of CO chemisorption over Pd catalysts. c,d) Peak area integral of CO adsorption sites and CO₂. Gas phase CO band was subtracted from atop Pd⁰-CO sites.

surface of both catalysts in the spectra range between 1650 and 1150 cm⁻¹ during the first 30 s of CO exposure (see supplementary materials Fig. 1), indicating that surface oxygen species might be responsible for the formation of carbonate species [36].

The DRIFTS experiments reveal that oxidized Pd on CeO₂ can be reduced immediately in the first 30 s of CO exposure, forming Pd⁰ sites. In the case of Pd/MC, Pd²⁺ species do not get reduced during CO adsorption immediately. Since there is no gas phase O₂ fed to the DRIFTS cell, Pd⁰ is likely get re-oxidized by the lattice oxygen from the supports, which is in agreement with the re-oxidation behavior observed on the Pt/CeO₂ catalysts [37]. However, this re-oxidation on MC might be fast enough that the CO-Pd⁰ band could not be detected until the first 60 s of CO exposure, while there is still CO₂ production during this time. Appearance of the bands for the adsorbed CO on bridge and hollow sites after 120 s implies that MC can suppress the formation of adjacent metallic Pd-Pd sites. The higher re-oxidation capability of MC again can be attributed to the decreased formation energy of oxygen vacancies [31,32]. In addition, many studies reported that a charge transfer exists between PGM and CeO₂ [38–40], which could be coupled with oxygen transfer for low temperature CO oxidation activity. During the charge

transfer, Pd⁰ can transfer electrons to Ce⁴⁺, forming oxidized Pd and Ce³⁺ with oxygen vacancy, which can facilitate the release of lattice oxygen [38–40].

3.5. Reducibility of lattice oxygen

Reducibility of the lattice oxygen is investigated through H₂-TPR and CO/O₂ transient experiments. As shown in Fig. 8, the CeO₂ support exhibits two weak reduction peaks at around 500 °C and 800 °C, which can be attributed to the reduction of surface and bulk oxygen species, respectively [41]. The reduction profile of MC also shows two reduction peaks at lower temperatures than CeO₂. The first reduction peak of MC at around 250 °C corresponds to the reduction of Mn⁴⁺ to Mn²⁺/Mn³⁺, while the second peak at 370 °C can be attributed to the reduction of Mn²⁺/Mn³⁺ to Mn²⁺ and surface oxygen of CeO₂ [42]. The downshift in the reduction temperature after Mn doping might be due to the facile redox cycle and enhanced oxygen mobility [42]. It is also possible that dissolution of MnO_x-CeO₂ solid solution during H₂ reduction can affect the TPR profile. At lower reduction temperatures, e.g. 250 °C, the reduced Mn³⁺ may not necessarily separate from the CeO₂ fluorite

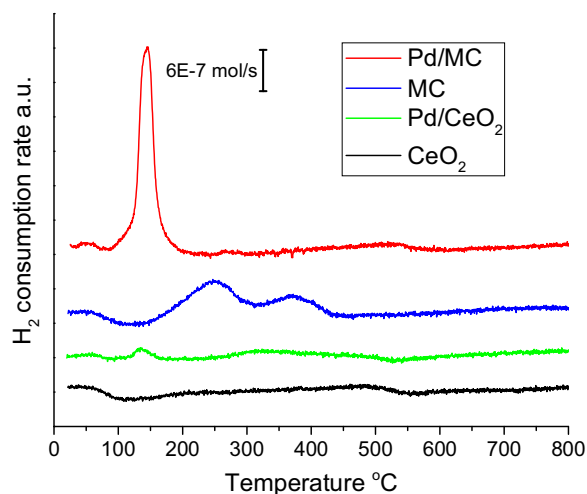


Fig. 8. H_2 -TPR profiles of the CeO_2 , MC, and 1 wt% Pd catalysts.

structure, as reported after multiple H_2 - O_2 redox cycles [43]. However, it is possible that further reduction of Mn^{3+} to Mn^{2+} at 370°C might lead to a distortion in the fluorite lattice and eventually a phase separation. With the addition of Pd, 1 wt% Pd/ CeO_2 shows a reduction peak at 140°C , which can be ascribed to the reduction of PdO to Pd^0 [18]. The amount of H_2 consumed at 140°C is calculated to be 2.1×10^{-5} mol. This value is close to the amount of Pd (1.9×10^{-5} mol), calculated using the actual metal loading reported in section 2.1. The similarities in between the amount of H_2 consumed and the Pd content in the CeO_2 was also reported in the literature and is consistent with this work [44]. Based on the XPS and XAS results, we can also assume that all the Pd in the sample is oxidized to PdO . In the case of Pd/MC, the reduction peaks of the MC support observed at 250°C and 370°C disappear and a single reduction peak at 140°C with a total H_2 consumption of 4.1×10^{-4} mol is observed. This value is approximately 20 times bigger than the actual Pd amount on MC and close to the measured H_2 consumption of the MC support (4.3×10^{-4} mol). The similar amounts of H_2 consumed over Pd/MC and MC indicate that the bulk lattice oxygen of MC can be extracted and reacted at lower temperatures in the presence of Pd. The disappearance of the high temperature reduction peaks on the Pd/MC sample can be attributed to lattice oxygen reduction by H_2 spillover or oxygen reverse spillover from the support [13–15,45], which is also pronounced in the XAS and DRIFTS experiments. As shown in Fig. 7, the lack of CO - Pd^0 bands during the first 30 s of CO exposure reveals that the Pd^{2+} can be reduced by CO and then re-oxidized by the lattice oxygen from the MC support. Such oxygen reverse spillover contributes to the stabilization of Pd^{2+} during CO oxidation, as shown in Fig. 6.

In addition to the H_2 -TPR experiments, CO/O_2 transient pulse experiments were carried out at 50°C to evaluate the oxygen transfer of the Pd deposited CeO_2 and MC supports. As shown in Fig. 9, CO_2 is immediately produced on Pd/ CeO_2 and Pd/MC upon exposure to CO only, which is consistent with the DRIFTS experiments. The initial CO pulse produces 1.5×10^{-4} mol of CO_2 on Pd/MC, which is much higher than the amount of Pd^{2+} (ca. 2.0×10^{-5} mol) on the catalyst, indicating that the lattice oxygen from the support must be involved in the reduction. On the other hand, a much smaller amount of CO_2 (8.1×10^{-6} mol) is produced over Pd/ CeO_2 , suggesting that the lattice oxygen is less likely to react with CO at low temperatures. Upon exposure to O_2 , CO_2 is produced more due to the decomposition of carbonate species on the support and reaction of chemisorbed CO on Pd [46,47]. After four pulse cycles of CO and O_2 injection, CO_2 production stabilizes at around 2.0×10^{-5} mol and 7.4×10^{-6} mol for Pd/MC and Pd/ CeO_2 , respec-

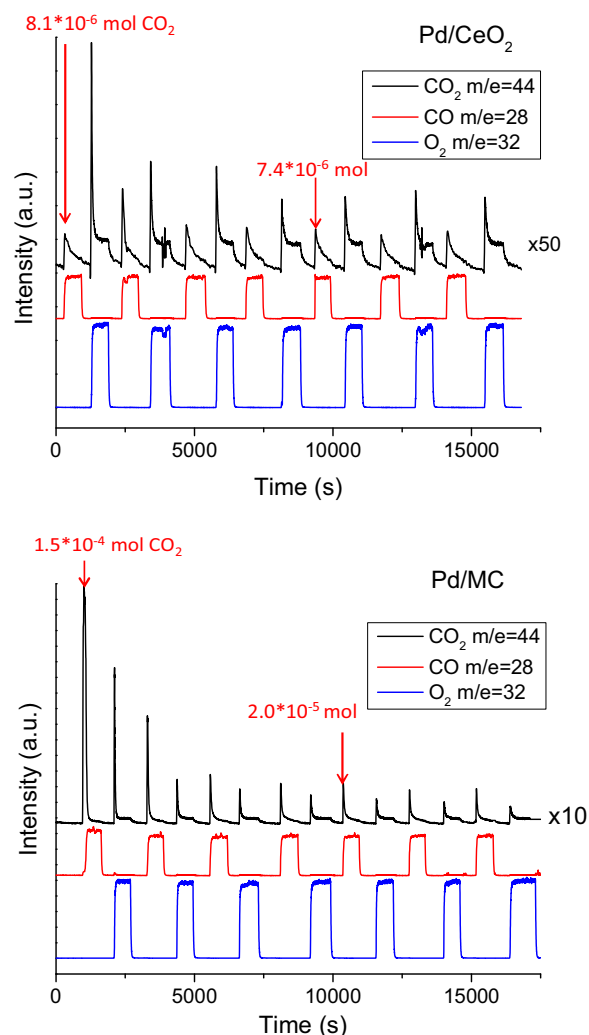


Fig. 9. CO/O_2 transient reaction profile of 1 wt% Pd/ CeO_2 and Pd/MC. Evolution of CO_2 , O_2 , CO signals were monitored as a function of time.

tively. The ratio of the steady state CO_2 production (2.7) of Pd/MC and Pd/ CeO_2 at 50°C in the CO/O_2 transient pulse experiments is consistent with one (2.5) in the CO oxidation experiments. This suggests that CO adsorption is not the rate limiting step for CO oxidation. The low CO_2 production on Pd/ CeO_2 implies that Pd/MC can release lattice oxygen easier than Pd/ CeO_2 . The decrease in steady state CO_2 production of Pd/ CeO_2 and Pd/MC might be due to the limited oxygen transfer rate or accumulation of different carbonate species on the surface that partially block adsorption of O_2 [48].

4. Conclusions

In this work, the high activity of Pd/MC for low temperature CO oxidation is investigated through a series of characterization experiments. Our results indicate that highly dispersed PdO species can form on freshly calcined CeO_2 and MC supports. In-situ XAS experiments reveal that Pd^{2+} species are reduced to Pd^0 on CeO_2 during CO oxidation, while Pd maintains its initial oxidation state on MC. The presence of stable Pd^{2+} species on MC shows that Pd is re-oxidized by the lattice oxygen of MC.

Participation of lattice oxygen in the low temperature CO oxidation is also supported by the H_2 -TPR and CO/O_2 transient pulse experiments. Despite the similar H_2 reduction temperatures observed for both Pd/ CeO_2 and Pd/MC, the higher amount of H_2 consumed on Pd/MC indicates that more lattice oxygen of MC

can be extracted at lower temperatures. Similarly, CO/O₂ transient pulse experiments imply that Pd/MC shows higher reducibility at 50 °C in the presence of CO compared to one for Pd/CeO₂. Smaller amount of CO₂ produced on Pd/CeO₂ suggests that the lattice oxygen in the CeO₂ support is less likely to react with CO at 50 °C. In the case of Pd/MC, a higher amount of oxygen is replenished and transferred from the gas phase O₂, leading to high CO oxidation activity at low temperatures.

Acknowledgments

This work was supported by the South Carolina SmartState Center for Strategic Approaches to the Generation of Electricity (SAGE), a SPARC graduate research grant from University of South Carolina. The authors thank Dr. Oleg S. Alexeev for his assistance running the XAS experiments.

This research was performed, in part, using instrumentation (FEI Talos F200X S/TEM) provided by the Department of Energy, Office of Nuclear Energy, Fuel Cycle R&D Program and the Nuclear Science User Facilities. The authors thank Dr. Michael J. Lance for elemental mapping and imaging of particles.

Appendix A. Supplementary data

Supplementary data associated with this article can be found, in the online version, at <http://dx.doi.org/10.1016/j.apcatb.2017.01.020>.

References

- [1] M. Shelef, R.W. McCabe, *Catal. Today* 62 (2000) 35–50.
- [2] EPA, <https://www3.epa.gov/airquality/carbonmonoxide/>.
- [3] E.J. Peterson, A.T. DeLaRiva, S. Lin, R.S. Johnson, H. Guo, J.T. Miller, J. Kwak, C. Peden, B. Kiefer, L.F. Allard, F.H. Ribeiro, A.K. Datye, *Nat. Commun.* 5 (2014) 4885–4896.
- [4] J.C. Summers, J.E. Sawyer, A.C. Frost, *ACS Symp. Pap.* 495 (1992) 98–114.
- [5] J.C. Summers, S.A. Ausen, *J. Catal.* 58 (1979) 131–143.
- [6] G.B. Balazs, R.S. Glass, *Solid State Ionics* 76 (1995) 155–162.
- [7] M.S. Hegde, P. Bera, *Catal. Today* 253 (2015) 40–50.
- [8] D.O. Scanlon, B.J. Morgan, G.W. Watson, *Phys. Chem. Chem. Phys.* 13 (2011) 4279–4284.
- [9] S. Colussi, A. Gayen, M.F. Camellone, M. Boaro, J. Llorca, S. Fabris, A. Trovarelli, *Angew. Chem. Int. Ed.* 48 (2009) 8481–8484.
- [10] S. Hinokuma, H. Fujii, M. Okamoto, K. Ikeue, M. Machida, *Chem. Mater.* 22 (2010) 6183–6190.
- [11] R.V. Gulyaev, T. Kardash, S.E. Malykhin, O.A. Stonkus, A.S. Ivanova, A.I. Boronin, *Phys. Chem. Chem. Phys.* 16 (2014) 13523–13539.
- [12] J.A. Kurzman, L.M. Misch, R. Seshadri, *Dalton Trans.* 42 (2013) 14653–14667.
- [13] A. Neitzel, A. Figueroba, Y. Lykhach, T. Skála, M. Vorokhta, N. Tsud, S. Mehl, K. Ševčíková, K.C. Prince, K.M. Neyman, V. Matolín, J. Libuda, *J. Phys. Chem. C* 120 (2016) 9852–9862.
- [14] Y. Lykhach, A. Figueroba, M. Camellone, A. Neitzel, T. Skála, F.R. Negreiros, M. Vorokhta, N. Tsud, K.C. Prince, S. Fabris, K.M. Neyman, V. Matolín, J. Libuda, *Phys. Chem. Chem. Phys.* 18 (2016) 7672–7679.
- [15] L. Meng, A.P. Jia, J.Q. Lu, L.F. Luo, W.X. Huang, M.F. Luo, *J. Phys. Chem. C* 115 (2011) 19789–19796.
- [16] L. Meng, J.J. Lin, Z.Y. Pu, L.F. Luo, A.P. Jia, W.X. Huang, M.F. Luo, J.Q. Lu, *Appl. Catal. B* 119 (2012) 117–122.
- [17] H.S. Gandhi, G.W. Graham, R.W. McCabe, *J. Catal.* 216 (2003) 433–442.
- [18] M.F. Luo, Z.Y. Hou, X.X. Yuan, X.M. Zheng, *Catal. Lett.* 50 (1998) 205–209.
- [19] Z.Q. Zou, M. Meng, Y.Q. Zha, *J. Phys. Chem. C* 114 (2010) 468–477.
- [20] C. Wang, E. Sasmaz, C. Wen, J. Lauterbach, *Catal. Today* 258 (2015) 481–486.
- [21] X.M. Zhang, Y.Q. Deng, P. Tian, H.H. Shang, J. Xu, Y.F. Han, *Appl. Catal. B* 191 (2016) 179–191.
- [22] C. Wang, A.J. Binder, T.J. Toops, J. Lauterbach, E. Sasmaz, *Emiss. Control Sci. Technol.* (2016) 1–10, <http://dx.doi.org/10.1007/s40825-016-0056-9>.
- [23] R.E. Jentoft, S.E. Deutsch, B.C. Gates, *Rev. Sci. Instrum.* 67 (1996) 2111–2112.
- [24] B. Ravel, M. Newville, *J. Synchrotron. Radiat.* 12 (2005) 537–541.
- [25] K.R. Priolkar, P. Bera, P.R. Sarode, M.S. Hegde, S. Emura, R. Kumashiro, N.P. Lalla, *Chem. Mater.* 14 (2002) 2120–2128.
- [26] A.I. Boronin, E.M. Slavinskaya, I.G. Danilova, R.V. Gulyaev, Y.I. Amosov, P.A. Kuznetsov, I.A. Polukhina, S.V. Koscheev, V.I. Zaiikovskii, A.S. Noskov, *Catal. Today* 144 (2009) 201–211.
- [27] B. Corain, G. Schmid, *Metal Nanoclusters in Catalysis and Materials Science: The Issue of Size Control*, Elsevier, 2008.
- [28] S. Penner, P. Bera, S. Pedersen, L.T. Ngo, J. Harris, C.T. Campbell, *J. Phys. Chem. B* 110 (2006) 24577–24584.
- [29] W.F. Engelhoff, *Surf. Sci. Rep.* 6 (1987) 253–415.
- [30] C.I. Hiley, J.M. Fisher, D. Thompson, R.J. Kashtiban, J. Sloan, R.I. Walton, *J. Mater. Chem. A* 3 (2015) 13072–13079.
- [31] S. Imamura, M. Shono, N. Okamoto, A. Hamada, S. Ishida, *Appl. Catal. A* 142 (1996) 279–288.
- [32] W. Cen, Y. Liu, Z. Wu, H. Wang, X. Weng, *Phys. Chem. Chem. Phys.* 14 (2012) 5769–5777.
- [33] A. Satsuma, K. Osaki, M. Yanagihara, J. Ohya, K. Shimizu, *Appl. Catal. B* 132 (2013) 511–518.
- [34] T. Ressler, J. Wong, J. Roos, I.L. Smith, *Environ. Sci. Technol.* 34 (2000) 950–958.
- [35] S. Royer, D. Duprez, *ChemCatChem* 3 (2011) 24–65.
- [36] C. Li, Y. Sakata, T. Arai, K. Domen, K. Maruya, T. Onishi, *J. Chem. Soc., Faraday Trans. I* 85 (1989) 929–943.
- [37] W. Lin, A.A. Herzog, C.J. Kiely, I.E. Wachs, *J. Phys. Chem. C* 112 (2008) 5942–5951.
- [38] A. Bruix, J.A. Rodriguez, P.J. Ramirez, S.D. Senanayake, J. Evans, J.B. Park, D. Stacchiola, P. Liu, J. Hrbek, F. Illas, *J. Am. Chem. Soc.* 134 (2012) 8968–8974.
- [39] Y. Choi, M. Scott, T. Söhnel, H. Idriss, *Phys. Chem. Chem. Phys.* 16 (2014) 22588–22599.
- [40] J.A. Farmer, C.T. Campbell, *Science* 329 (2010) 933–936.
- [41] J.Y. Luo, M. Meng, J.S. Yao, X.G. Li, Y.Q. Zha, X. Wang, T.Y. Zhang, *Appl. Catal. B* 87 (2009) 92–103.
- [42] X.F. Tang, J.L. Chen, X.M. Huang, Y.D. Xu, W.J. Shen, *Appl. Catal. B* 81 (2008) 115–121.
- [43] P. Zhang, H. Lu, Y. Zhou, L. Zhang, Z. Wu, S. Yang, H. Shi, Q. Zhu, Y. Chen, S. Dai, *Nat. Commun.* 6 (2015) 8446–8455.
- [44] Y. Su, Z. Tang, W. Han, P. Zhang, Y. Song, G. Lu, *Cryst. Eng. Comm.* 16 (2014) 5189–5197.
- [45] L. Lan, S. Chen, M. Zhao, M. Gong, Y. Chen, *J. Mol. Catal. A* 394 (2014) 10–21.
- [46] S. Sharma, S. Hilaire, J.M. Vohs, R.J. Gorte, H.W. Jen, *J. Catal.* 90 (2000) 199–204.
- [47] C. Chen, J.J. Cao, M. Cargnello, P. Fornasiero, R.J. Gorte, *J. Catal.* 306 (2013) 109–115.
- [48] P. Konova, A. Naydenov, C. Venkov, D. Mehandjiev, D. Andreeva, T. Tabakova, *J. Mol. Catal. A: Chem.* 213 (2004) 235–240.